An immersed boundary method for the incompressible Navier–Stokes equations in complex geometry

Tony W. H. Sheu[*,†,‡], H. F. Ting and R. K. Lin[§]

Department of Engineering Science and Ocean Engineering, National Taiwan University, No. 1, Sec. 4, Roosevelt Road, Taipei, Taiwan 106, Republic of China

SUMMARY

A nodally exact convection–diffusion–reaction scheme developed in Cartesian grids is applied to solve the flow equations in irregular domains within the framework of immersed boundary (IB) method. The artificial momentum forcing term applied at certain points in the flow and inside the body of any shape allows the imposition of no-slip velocity condition to account for the body of complex boundary. Development of an interpolation scheme that can accurately lead to no-slip velocity condition along the IB is essential since Cartesian grid lines generally do not coincide with the IB. The results simulated from the proposed IB method agree well with other numerical and experimental results for several chosen benchmark problems. The accuracy and fidelity of the IB flow solver to predict flows with irregular IBs are therefore demonstrated. Copyright © 2007 John Wiley & Sons, Ltd.

1. INTRODUCTION

One of the major issues in flow simulations is the ability to handle complex geometries. In many practical problems, simulation of nonlinear flow system, subjected to moving or deformable boundaries, is computationally difficult due to the inevitable mesh regeneration at every time step. In the past, body-fitted and immersed boundary (IB) methods have been successfully applied to

WILEY InterScience®
DISCOVER SOMETHING GREAT

predict this type of fluid flows in complex domains. Body-fitted method, which generates the curvilinear structured or unstructured grids that conform to the body, proceeds to distribute surface grids on the entire boundary. This is followed by generating the meshes in the domain occupied by the fluid through, for example, the elliptic differential equations with the surface grid coordinates considered as the boundary conditions. Imposition of boundary conditions in curvilinear grids that conform to the boundary is greatly simplified and the flow solver can, at the same time, yield adequate prediction accuracy. Grid quality of mesh generation becomes, however, a major concern. Depending on the degree of geometrical complexity, one may resort to a multiblock approach to generate meshes in several geometrically more simple subdomains. Moreover, an indispensable use of coordinate transformations to map the governing equations in curvilinear coordinates involves calculation of several metric tensors and transformation Jacobians. The complexity resulting from the transformation of governing equations can very often deteriorate the convergence of flow calculation due to adverse impact on the stability. As an alternative to the use of generalized coordinate transformation, Peskin [1] developed the IB method, which enables to represent a body of any shape within a flow field by adding a forcing term to the governing equations, without the necessity of performing the mapping procedures. The forcing terms applied at certain nodal points in the flow simulate the effect of the body. This allows for the modeling of a body of any shape within the context of Cartesian grids. The developed IB method can therefore cope with the flow complexity but at the same time the solution accuracy can be retained in the fixed grid. Therefore, simulation of fluid flows over a moving or deformable object with complex geometry becomes possible in Cartesian grids without the need of generating time-varying meshes.

The concept of IB method was due to the pioneering work of Peskin [1], who simulated the blood flow in moving heart valves in the regular Eulerian fluid domain by representing the body within a flow field by virtue of a forcing term added to the working flow equations. The IB method can yield a singular force which can be calculated by the well-chosen discrete delta function on each Lagrangian marker. Recently, some new types of Peskin method have been proposed. Inspired by the work of Sirovich [2], Goldstein *et al.* [3] developed a virtual boundary method (feedback forcing method) in their prediction of the two-dimensional start-up flow fields around a circular cylinder, three-dimensional plane, and ribbed-turbulent channel. The idea of virtual boundary method is rooted in the introduced forcing term, which is governed by a feedback loop, to account for the solid body. The feedback forcing term added to the momentum equation allows imposition of a no-slip boundary within the flow field but can, however, induce high-frequency spurious oscillations, thereby considerably restricting the chosen time step and making the simulation of flow fields in complex domains very expensive. Saiki and Biringen [4] improved the virtual boundary method of Goldstein in their simulation of stationary and moving cylinders in a uniform flow at low Reynolds numbers ($Re \leqslant 400$). They could eliminate the spurious oscillations caused by the applied feedback forcing term at the boundary by employing the area-weighted average function for a better interpolation of the fluid velocity at the boundary points and an appropriate distribution of nodal boundary forces at these grid points.

The IB method is featured with the source term (or function) added to the equations of motion. The forcing function introduced for reproducing the effect of boundary could normally be implemented through two major ways. The resulting fundamental dichotomy in IB methods includes the continuous forcing approach and the discrete forcing approach. The first approach involves the inclusion of a forcing function into the continuous governing equations prior to the discretization of the differential equations. Since the constitutive equations can be directly incorporated into the formulation, application of continuous forcing method can give a sound physical basis for the

investigated flows with immersed elastic boundaries. It is therefore more suitable for the simulation of biological and multiparae flows rather than for flow simulations involving rigid bodies. Another advantage of applying the continuous forcing method is that the method can be formulated independent of the employed underlying spatial discretization. On the contrary, a forcing term is introduced after the equations being discretized for the discrete forcing approach. Hence, it can be expected that the discrete forcing approach is not as straightforward to be implemented as the continuous forcing approach. The forcing strategy, which is intimate in association with the employed discretization schemes, enables a sharper representation of the IB. Depending on the way of prescribing the boundary condition on the IB, the discrete forcing approach can be categorized into the indirect and direct boundary condition impositions. Two types of methods, known as the ghost-cell finite difference method and cut-cell finite element method, can fit into the methods of direct boundary condition imposition. The reader can refer to the review paper by Mittal and Iaccarino [5] for additional details. Since the current study investigates the flow over the stationary rigid body, only some of the discrete forcing methods will be dealt with below.

Mohd-Yusof [6] introduced a momentum forcing term that does not affect the stability of the discrete-time equation. The need of using a small computational time step, which is regarded as an important advantage of this method over other previous methods, is therefore avoided. Fadlun *et al.* [7] further implemented the approach of Mohd-Yusof in staggered grids and showed that the momentum forcing suggested by Mohd-Yusof is more effective than the feedback forcing in their three-dimensional flow simulations.

Ye *et al.* [8] proposed a so-called Cartesian grid method in non-staggered grids to simulate the unsteady, incompressible Navier–Stokes equations in the physical domain with complex IB. In their cut-cell method, it is of primary importance to satisfy the underlying conservation for the cells in the vicinity of the IB. In the whole computational domain, a finite-volume method of second-order accuracy is applied together with the two-step fractional-step procedure. Near the IB, an interpolation procedure of second-order spatial accuracy is used.

This paper is organized as follows. We describe in Section 2 the working equations for the incompressible Navier–Stokes equations cast in the primitive variable form. The IB method implemented with the accurate interpolation scheme will be proposed in Section 3 for the evaluation of momentum forcing on the body surface (IB) or inside the body. Section 4 presents the two-dimensional convection–diffusion–reaction (CDR) scheme to obtain the Navier–Stokes solution in non-staggered grids without producing oscillatory pressures. Section 5 verifies the proposed steady and transient Navier–Stokes solvers. For the fidelity of the numerical model, two benchmark problems are considered. In order to verify the IB method, two classical problems will be investigated in Section 6. In Section 7, some concluding remarks are drawn.

2. GOVERNING EQUATIONS

In this study, we will restrict our attention to the incompressible viscous flow equations, which are governed by the following continuity and Navier–Stokes equations:

$$\nabla \cdot \mathbf{u} = 0 \tag{1}$$

$$\frac{\partial \mathbf{u}}{\partial t} + (\mathbf{u} \cdot \nabla)\mathbf{u} = -\nabla p + \frac{1}{Re}\nabla^2 \mathbf{u} \tag{2}$$

Two primitive variables $\mathbf{u}$, p will be sought subject to the divergence-free velocity field at $t = 0$ and the prescribed boundary velocity. All lengths have been normalized by L, the velocity components by u_∞, the time by L/u_∞, and the pressure by ρu_∞^2, where ρ denotes the fluid density. The Reynolds number, $Re(\equiv \rho u_\infty L/\mu)$, shown above is appeared as the consequence of the chosen normalization.

Momentum conservation equations can be solved along with the divergence-free constraint equation (continuity equation (1)) to unconditionally ensure fluid incompressibility condition. Despite the widespread use of the coupled solution algorithm to solve the incompressible flow equations, the distribution of eigenvalues for the resulting matrix equation may make the calculation of incompressible flow solutions very difficult using a computationally less expensive iterative solver [9]. Besides this disadvantage, the peripheral storage for the system of matrix equations may exceed the available computer power and disk space. For overcoming this drawback, the well-known pressure Poisson equation approach [10] will be applied in this study to eliminate the pressure gradient terms from the momentum equations by performing a curl operator to the momentum equations. The resulting Poisson equation for the pressure unknown can be derived as follows in lieu of the divergence-free continuity equation (1):

$$\nabla^2 p = \nabla \left[-\frac{\partial \mathbf{u}}{\partial t} + \frac{1}{Re}\nabla^2 \mathbf{u} - (\mathbf{u} \cdot \nabla)\mathbf{u} \right] \tag{3}$$

In other words, the pressure values can be determined from the continuity constraint equation or the continuity equation can be considered as an implicit equation for pressure. The above elliptic equation will be solved subject to the Neumann-type boundary condition given by

$$\frac{\partial p}{\partial n} = \left(-\frac{\partial \mathbf{u}}{\partial t} + \frac{1}{Re}\nabla^2 \mathbf{u} - (\mathbf{u} \cdot \nabla)\mathbf{u} \right) \cdot \mathbf{n} \tag{4}$$

where $\mathbf{n}$ denotes the unit outward normal vector to the domain boundary.

3. IMMERSED BOUNDARY METHOD

Fluid flow over a body can exert a force on the no-slip surface, which will, in turn, apply a force with the magnitude and direction opposing the local flow such that the fluid flow can be brought to rest on the body surface [3]. In other words, introduction of a body force to the momentum equations at certain points in the flow can simulate the effect of the investigated body. Based on this idea, the IB method can mimic the complex body through a suitable artificial force introduced to the momentum equations. The resulting momentum equation with the appropriately prescribed forcing term $\mathbf{f}$ at certain points in the vicinity of IB can be written as

$$\frac{\partial \mathbf{u}}{\partial t} + (\mathbf{u} \cdot \nabla)\mathbf{u} = -\nabla p + \frac{1}{Re}\nabla^2 \mathbf{u} + \mathbf{f} \tag{5}$$

As the name of the discrete-time momentum forcing method indicates, the forcing term $\mathbf{f}$ shown in Equation (5) can be directly computed from the following discrete-time momentum equation:

$$\frac{\mathbf{u}^{n+1} - u^n}{\Delta t} + (\mathbf{u} \cdot \nabla)\mathbf{u} = -\nabla p + \frac{1}{Re}\nabla^2 \mathbf{u} + \mathbf{f} \tag{6}$$

Note that the momentum forcing $\mathbf{f}$, which is applied only on the body surface or inside the body, should be calculated at each time step. When the grid line coincides with the IB, the momentum forcing term is specified in a way to make the velocity magnitude to be equal to $\mathbf{V}_\Omega$ at this point. For the forcing point inside the body and nearest the boundary, the momentum forcing term needs to be specified such that the normal and tangential velocity components along the boundary are equal in magnitude but opposite in direction to the velocity components at the corresponding point outside the body. When the boundary surface is not aligned with the grid plane, the momentum forcing term will act only on the points nearest to the IB. An interpolation for the momentum forcing is therefore required so that the forcing term can render a velocity that is approximately equal to $\mathbf{V}_\Omega$ at the IB

$$\mathbf{f} = -\mathrm{RHS} + \frac{\mathbf{V}_\Omega - u^n}{\Delta t} \quad \text{on } \Omega \tag{7}$$

In the above, Δt denotes the time increment and $\mathbf{V}_\Omega$ represents the specified velocity along the IB. Note that the right-hand side (RHS) shown above is composed of the pressure gradient, convection and diffusion terms in the momentum equations. For the case with a stationary solid body, $\mathbf{V}_\Omega = 0$ will be specified along the boundary.

Imposition of nodal forces at the IBs is the key issue in developing an IB method. In general, the forcing points are not necessary to lie on the IB but are rather present inside the body. Thus, an interpolation procedure is required and the employed scheme for interpolating the velocity in the solid–fluid cell determines the degree of accuracy of the employed scheme.

The interpolation procedures due to Li and Wang [11] will be described firstly. Let P shown in Figure 1(a) be a point along the IB, at which no-slip boundary condition is prescribed. The nearest interior point A has only one fluid-neighbor point (node B). For this case, U_A and U_B can be calculated linearly from the nodal value of U_D and the no-slip velocity at P

$$U_A = -\frac{h_a}{h_d} U_D \quad \text{and} \quad U_B = -\frac{h_b}{h_d} U_D \tag{8}$$

In the above, h_a, h_b, h_d are denoted as the distances between the points A, B, D, and P, respectively. In Figure 1(b), the interior point A has two fluid-neighbor points B and D. Let u be approximated by $a_1 + a_2 x + a_3 y + a_4 xy$, then u_A–u_P can be expressed as follows:

$$\begin{aligned}
u_A &= a_1 + a_2 x_A + a_3 y_A + a_4 x_A y_A \\
u_B &= a_1 + a_2 x_B + a_3 y_B + a_4 x_B y_B \\
u_C &= a_1 + a_2 x_C + a_3 y_C + a_4 x_C y_C \\
u_D &= a_1 + a_2 x_D + a_3 y_D + a_4 x_D y_D \\
u_P &= a_1 + a_2 x_P + a_3 y_P + a_4 x_P y_P
\end{aligned} \tag{9}$$

One can then solve the following matrix to obtain the values of a_1–a_4 and, in turn, u_P from:

$$\begin{bmatrix} 1 & x_A & y_A & x_A y_A \\ 1 & x_B & y_B & x_B y_B \\ 1 & x_C & y_C & x_C y_C \\ 1 & x_D & y_D & x_D y_D \end{bmatrix} \cdot \begin{bmatrix} a_1 \\ a_2 \\ a_3 \\ a_4 \end{bmatrix} = \begin{bmatrix} u_A \\ u_B \\ u_C \\ u_D \end{bmatrix}$$
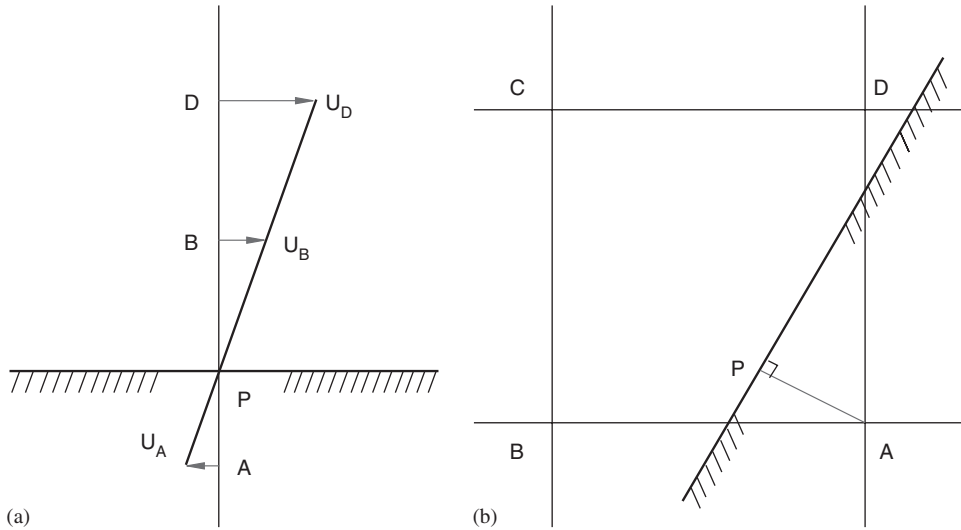
Figure 1. Schematic of the interpolation schemes: (a) linear interpolation and (b) bilinear interpolation.

In most of the problems, the no-slip velocity condition at P is known and we can always use u_B, u_C, u_D, and u_P to calculate u_A. In other words, the value of u_A can be computed in a way to satisfy the no-slip condition on the IB (point P). In order to save the CPU time, u_P is derived as

$$u_P = \frac{[(u_D \cdot \Delta x_1 + u_C \cdot \Delta x_2)\Delta y_2 + (u_A \cdot \Delta x_1 + u_B \cdot \Delta x_2)\Delta y_1]}{[(\Delta x_1 + \Delta x_2)(\Delta y_1 + \Delta y_2)]} \quad (10)$$

where $\Delta x_1 = x_P - x_B$, $\Delta x_2 = x_A - x_P$, $\Delta y_1 = y_D - y_P$, $\Delta y_2 = y_P - y_A$ are shown in Figure 2. By setting $u_P = 0$ in Equation (10), u_A can be derived as

$$u_A = \frac{-(u_D \cdot \Delta x_1 + u_C \cdot \Delta x_2)\Delta y_2}{\Delta y_1 \cdot \Delta x_1} - \frac{(u_B \cdot \Delta x_2)}{\Delta x_1} \quad (11)$$

The following five equations can then be rewritten as:

$$u_A = a_1 + a_2(x_P + \Delta x_2) + a_3(y_P - \Delta y_2) + a_4(x_P + \Delta x_2)(y_P - \Delta y_2)$$
$$u_B = a_1 + a_2(x_P - \Delta x_1) + a_3(y_P - \Delta y_2) + a_4(x_P - \Delta x_1)(y_P - \Delta y_2)$$
$$u_C = a_1 + a_2(x_P - \Delta x_1) + a_3(y_P + \Delta y_1) + a_4(x_P - \Delta x_1)(y_P + \Delta y_1) \quad (12)$$
$$u_D = a_1 + a_2(x_P + \Delta x_2) + a_3(y_P + \Delta y_1) + a_4(x_P + \Delta x_2)(y_P + \Delta y_1)$$
$$u_P = a_1 + a_2 x_P + a_3 y_P + a_4 x_P y_P$$

This is followed by computing the value of u_P, which is equal to

$$a_1 + a_2 x_P + a_3 y_P + a_4 x_P y_P = \frac{(u_D \cdot \Delta x_1 + u_C \cdot \Delta x_2)\Delta y_2 + (u_A \cdot \Delta x_1 + u_B \cdot \Delta x_2)\Delta y_1}{(\Delta x_1 + \Delta x_2)(\Delta y_1 + \Delta y_2)} \quad (13)$$

In the IB method, development of an interpolation scheme to accurately yield the no-slip condition on the IB is very important because the grid lines are not necessarily aligned with the
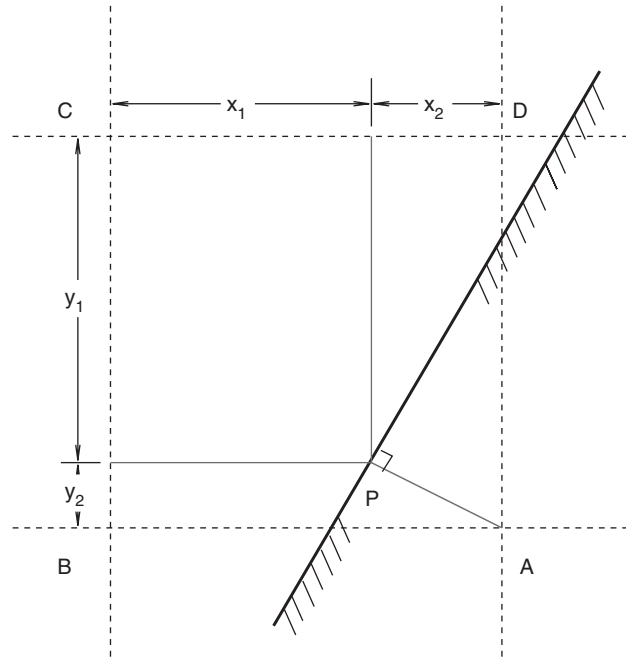
Figure 2. Schematic of the bilinear interpolation and the definitions of $x_1 \sim y_2$.

IB. Therefore, a reliable interpolation technique for evaluating the momentum forcing term on the body surface or inside the body will be presented here. The main idea of the proposed direct forcing method is to capture the body shape, which is normally not smooth because only one boundary no-slip point is invoked in each solid–fluid (**s–f**) cell and the number of computational grids is finite. Therefore, we are motivated to employ more boundary no-slip points to more accurately represent the body shape.

Within the context of bilinear interpolation scheme, the corrected velocity ($\mathbf{u}^{**}$) at point 2 can be calculated from the velocities ($\mathbf{u}^*$) obtained at three neighboring points 1, 3, 4 and one at the no-slip point **b**. If the biquadratic interpolation scheme is considered, the number of computational grids along one direction needs to be doubled and the boundary no-slip points are considerably increased. For the sake of computational efficiency, we propose a 'mimic quadratic interpolation scheme'. In Figure 3, the solid and dotted lines represent the coarse and fine grids, respectively. The notations 1–4 represent the grid points on the coarse grids, 5–9 are the grid points on the fictitious fine grids. '◯' is the forcing point on the coarse grid, '∘' denotes the impermanent mimic forcing points on the fictitious fine grids, '•' represents the no-slip point which is extended from the forcing points normal to the IB.

The proposed quadratic interpolation scheme is to correct the velocities ($\mathbf{u}^*$) at the forcing points that are located on the fictitious fine grids in the **s–f** cell as the points numbering with 5, 6, 8. This is followed by using the temporarily corrected velocities ($\mathbf{u}^t$) at points 5, 6, 8, intermediate velocities ($\mathbf{u}^*$) at points 1, 3, 4, 7, 9, and no-slip point on the coarse grid **b** to interpolate the final corrected velocity ($\mathbf{u}^{**}$) at point 2. The computational procedures are as follows. The first step is to calculate the intermediate velocity $\mathbf{u}^*$. Here, this velocity is determined in the entire
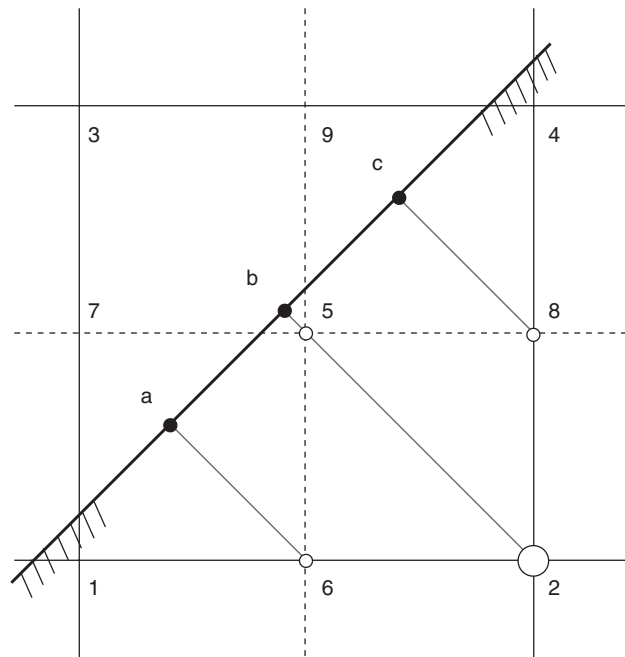
Figure 3. Schematic of the quadratic interpolation.

computational domain regardless of the position of the immersed body:

$$\frac{\mathbf{u}^* - \mathbf{u}^n}{\Delta t} + (\mathbf{u}^n \cdot \nabla)\mathbf{u}^n = -\nabla p + \frac{1}{Re}\nabla^2 \mathbf{u}^n \tag{14}$$

The second step is to correct the intermediate velocity $\mathbf{u}^*$ using the proposed 'quadratic interpolation method'. In order to satisfy the no-slip condition, the temporarily corrected velocities $\mathbf{u}^t$ for the forcing points on the fictitious fine mesh are expressed as

$$\mathbf{u}^t = \begin{cases} 0 & \text{on IB} \\ f(\mathbf{u}^*) & \text{in s–f cell} \\ \mathbf{u}^* & \text{in fluid} \end{cases}$$

where $f(\mathbf{u}^*)$ is a function of the intermediate velocities $\mathbf{u}^*$ as mentioned before. Take Figure 3 as an example, the corrected velocities $\mathbf{u}^t$ in **s–f** cell are given as follows:

$$\mathbf{u}^t = \begin{cases} \mathbf{u}_5^t, & f(\mathbf{u}_3^*, \mathbf{u}_7^*, \mathbf{u}_9^*, \mathbf{u}_b) & \text{on point 5} \\ \mathbf{u}_6^t, & f(\mathbf{u}_1^*, \mathbf{u}_5^*, \mathbf{u}_7^*, \mathbf{u}_a) & \text{on point 6} \\ \mathbf{u}_8^t, & f(\mathbf{u}_4^*, \mathbf{u}_5^*, \mathbf{u}_9^*, \mathbf{u}_c) & \text{on point 8} \end{cases}$$

With the intermediate velocities $(\mathbf{u}_1^*, \mathbf{u}_3^*, \mathbf{u}_4^*, \mathbf{u}_7^*, \mathbf{u}_9^*)$, the temporarily corrected velocities $(\mathbf{u}_5^t, \mathbf{u}_6^t, \mathbf{u}_8^t)$ on the fictitious fine mesh, and the no-slip boundary point **b**, which is obtained from the original

coarse grids, the corrected velocity at point 2 takes the following functional form:

$$\mathbf{u}_2^{**} = f(\mathbf{u}_1^*, \mathbf{u}_3^*, \mathbf{u}_4^*, \mathbf{u}_6^*, \mathbf{u}_7^*, \mathbf{u}_9^*, \mathbf{u}_5^t, \mathbf{u}_6^t, \mathbf{u}_8^t, \mathbf{u}_b) \tag{15}$$

The third step imposes the forcing term $\mathbf{f}$ in $\mathbf{s}$–$\mathbf{f}$ cells. The velocity is made to have zero magnitude on the body surface. The presence of the prescribed forcing term implies that the updated velocity will be computed from

$$\frac{\mathbf{u}^{**} - \mathbf{u}^n}{\Delta t} + (\mathbf{u}^n \cdot \nabla)\mathbf{u}^n = -\nabla p + \frac{1}{Re}\nabla^2\mathbf{u}^n + \mathbf{f} \tag{16}$$

or

$$\mathbf{f} = -\text{RHS} + \frac{\mathbf{u}^{**} - \mathbf{u}^n}{\Delta t} \tag{17}$$

where $\mathbf{f} = (f_1, f_2)$. Note that RHS denotes the sum of the pressure gradient, convection, and diffusion terms in the momentum equations. The final step is to calculate $\mathbf{u}^{n+1}$. We can substitute $\mathbf{f}$ obtained from step 3 into the momentum equations to calculate $\mathbf{u}$ at the new time step $n + 1$.

4. DISCRETIZATION SCHEMES

4.1. Five-point scheme for convection–diffusion–reaction equation

In view of Equation (2), the following transport equation for the field variable $\phi(= u, v)$ will be chosen to describe the proposed discretization scheme:

$$(\mathbf{u} \cdot \nabla)\phi - k\nabla^2\phi + c\phi = f \tag{18}$$

Note that $\mathbf{u}$ ($\equiv (a, b)$) in the above equation is a vector with the constant velocity components a and b. Derivation of the discretization scheme starts with employing the following general solution for (18) so as to suppress the convective instability and to retain the prediction accuracy

$$\phi(x, y) = A_1 e^{\lambda_1 x} + A_2 e^{\lambda_2 x} + A_3 e^{\lambda_3 y} + A_4 e^{\lambda_4 y} + \frac{f}{c} \tag{19}$$

In the above, A_1–A_4 are four arbitrary constants. By substituting the above equation into Equation (18), we are led to derive λ_1–λ_4 in terms of a, b, k, and c as

$$\lambda_{1,2} = \frac{a \pm \sqrt{a^2 + 4ck}}{2k} \quad \text{and} \quad \lambda_{3,4} = \frac{b \pm \sqrt{b^2 + 4ck}}{2k} \tag{20}$$

The discrete five-point stencil equation at an interior node (i, j) is assumed to take the following form:

$$\left(-\frac{a}{2h} - \frac{m}{h^2} + \frac{c}{12}\right)\phi_{i-1,j} + \left(\frac{a}{2h} - \frac{m}{h^2} + \frac{c}{12}\right)\phi_{i+1,j} + 4\left(\frac{m}{h^2} + \frac{2c}{12}\right)\phi_{i,j}$$

$$+ \left(-\frac{b}{2h} - \frac{m}{h^2} + \frac{c}{12}\right)\phi_{i,j-1} + \left(\frac{b}{2h} - \frac{m}{h^2} + \frac{c}{12}\right)\phi_{i,j+1} = f_{i,j} \tag{21}$$

Derivation is followed by substituting $\phi_{i,j} = A_1 e^{\lambda_1 x_i} + A_2 e^{\lambda_2 x_i} + A_3 e^{\lambda_3 y_j} + A_4 e^{\lambda_4 y_j} + f/c$, $\phi_{i\pm 1,j} = A_1 e^{\pm\lambda_1 h} e^{\lambda_1 x_i} + A_2 e^{\pm\lambda_2 h} e^{\lambda_2 x_i} + A_3 e^{\lambda_3 y_j} + A_4 e^{\lambda_4 y_j} + f/c$ and $\phi_{i,j\pm 1} = A_1 e^{\lambda_1 x_i} + A_2 e^{\lambda_2 x_i} + A_3 e^{\pm\lambda_3 h} e^{\lambda_3 y_j} + A_4 e^{\pm\lambda_4 h} e^{\lambda_4 y_j} + f/c$ into Equation (21). These substitutions enable us to derive the undetermined coefficient m as

$$m = \left[\frac{ah}{2} \sinh \overline{\lambda_1} \cosh \overline{\lambda_2} + \frac{bh}{2} \sinh \overline{\lambda_3} \cosh \overline{\lambda_4} + \frac{ch^2}{12} (\cosh \overline{\lambda_1} \cosh \overline{\lambda_2} \right.$$

$$\left. + \cosh \overline{\lambda_3} \cosh \overline{\lambda_4} + 10) \right] \bigg/ (\cosh \overline{\lambda_1} \cosh \overline{\lambda_2} + \cosh \overline{\lambda_3} \cosh \overline{\lambda_4} - 2) \tag{22}$$

where

$$(\overline{\lambda_1}, \overline{\lambda_2}) = \left(\frac{ah}{2k}, \sqrt{\left(\frac{ah}{2k}\right)^2 + \frac{ch^2}{k}} \right) \quad \text{and} \quad (\overline{\lambda_3}, \overline{\lambda_4}) = \left(\frac{bh}{2k}, \sqrt{\left(\frac{bh}{2k}\right)^2 + \frac{ch^2}{k}} \right)$$

For the unsteady case, the model CDR equation takes the following form:

$$\phi_t + (\mathbf{u} \cdot \nabla)\phi - k\nabla^2 \phi + c\phi = f \tag{23}$$

We apply the semi-discretization scheme to approximate Equation (23), where the employed Euler time-stepping scheme given by $\phi_t = (\phi^{n+1} - \phi^n)/\Delta t$ yields the first-order accuracy. The resulting equation containing only the spatial derivatives is as follows:

$$\overline{u}\phi_x^{n+1} + \overline{v}\phi_y^{n+1} - \overline{k}\nabla^2 \phi^{n+1} + \overline{c}\phi^{n+1} = \overline{f} \tag{24}$$

The definitions of $\overline{u}$, $\overline{v}$, $\overline{k}$, and $\overline{c}$ are given by $\overline{u} = u\Delta t$, $\overline{v} = v\Delta t$, $\overline{k} = k\Delta t$, $\overline{c} = 1 + c\Delta t$, and $\overline{f} = f^{n+1}\Delta t + \phi^n$.

4.2. Compact scheme for pressure gradient term in collocated grids

Staggered grid approaches employed to solve the incompressible flow equations have long been known to be effective to suppress pressure oscillations arising from the even–odd coupling. This type of approaches can, however, increase the programming complexity. Discretization of differential equations in a domain where the velocities and pressure are stored at the same point will be employed in this study. The pressure gradient term ∇p in the momentum equations must be carefully approximated in the non-staggered mesh system to avoid the spurious pressure oscillations. Our underlying idea of eliminating the notorious even–odd decoupling solutions is to employ $p_{i,j}$ when approximating ∇p at an interior node (i, j). Instead of explicitly approximating $\partial p/\partial x|_{i,j}$, its value can be calculated implicitly with $\partial p/\partial x|_{i\pm 1,j}$. Define $F_{i,j}$ as $F_{i,j} = h\partial p/\partial x|_{i,j}$, where h denotes the uniform mesh size. The scheme employed to calculate the nodal values of F is based on the following implicit equation [12, 13]:

$$\alpha_1 F_{i+1,j} + \beta_1 F_{i,j} + \gamma_1 F_{i-1,j} = a_1(p_{i+2,j} - p_{i+1,j}) + a_2(p_{i+1,j} - p_{i,j})$$

$$+ a_3(p_{i,j} - p_{i-1,j}) + a_4(p_{i-1,j} - p_{i-2,j}) \tag{25}$$

The seven coefficients shown above can be obtained by expanding $F_{i\pm1,j}$ in Taylor series with respect to $F_{i,j}$, and $p_{i\pm1,j}$ and $p_{i\pm2,j}$ with respect to $p_{i,j}$. This is followed by substituting the resulting expansion equations into Equation (25), employing the definition for $F_{i,j}$ to derive a set of algebraic equations, and setting $\alpha_1 = \gamma_1$ due to the elliptic nature of the pressure field. The coefficients can then be determined as $\alpha_1 = \frac{1}{5}$, $\beta_1 = \frac{3}{5}$, $a_1 = \frac{1}{60}$, $a_2 = \frac{29}{60}$, $a_3 = \frac{29}{60}$, and $a_4 = \frac{1}{60}$. The equation for $F_{i,j}$ at a nodal point located immediately adjacent to the right boundary point is derived from Equation (25) under $\alpha_1 = a_1 = a_2 = 0$.

Throughout this study, the second-order derivative terms for the velocities are approximated by the compact scheme [12, 13]. Calculation of $\phi_{xx}|_{i,j}$, for example, is started by assuming $\phi_{xx}|_{i,j} = S_{i,j}/h^2$. The value of $S_{i,j}$ is then implicitly computed from

$$h^2(\alpha_3 S_{i+1,j} + \beta_3 S_{i,j} + \gamma_3 S_{i-1,j}) = c_1\phi_{i+2,j} + c_2\phi_{i+1,j} + c_3\phi_{i,j} + c_4\phi_{i-1,j} + c_4\phi_{i-2,j} \quad (26)$$

Expanding $S_{i\pm1,j}$ with respect to $S_{i,j}$ and $\phi_{i\pm1,j}$, $\phi_{i\pm2,j}$ with respect to $\phi_{i,j}$ in Taylor series and then substituting them into the expression for $S_{i,j}$. The values for $(\alpha_3, \beta_3, \gamma_3, c_1, c_2, c_3, c_4, c_5)$ can be obtained from the eight algebraic equations as $(1, \frac{11}{2}, 1, \frac{3}{8}, 6, -\frac{51}{4}, 6, \frac{3}{8})$.

Since the proposed CDR scheme will break down at $u_i = 0$ and $c_3 = 0$. Discretization of Equation (3) should be treated differently. One way of accurately approximating p_{xx} and p_{yy} is to employ Equation (26) at the conditions of $\alpha_3 = \gamma_3 = 0$. The rest of the free parameters will be determined using the same method described earlier. The resulting discrete equation for $\nabla^2 p$ at an interior point (i, j) is given by

$$\nabla^2 p|_{i,j} = (p_{i+1,j+1} + p_{i-1,j+1} + p_{i+1,j-1} + p_{i-1,j-1}) - 20p_{i,j}$$

$$+ 4(p_{i+1,j} + p_{i-1,j} + p_{i,j+1} + p_{i,j-1}) \quad (27)$$

The quality of the approximation scheme for Equation (4) depends highly on the first derivative terms shown in the RHS. Depending on the sign of u, the value of u_x at the left boundary is obtained by setting $\alpha_3 = \gamma_3 = 0$ in Equation (26). The remaining coefficients are determined as $\beta_3 = 1$, $c_1 = -\frac{1}{12}$, $c_2 = \frac{4}{3}$, $c_3 = -\frac{5}{2}$, $c_4 = \frac{4}{3}$, and $c_5 = -\frac{1}{12}$.

5. VERIFICATION OF THE NAVIER–STOKES SOLVER

To verify the proposed Navier–Stokes solver, two benchmark problems are chosen in this study.

5.1. Lid-driven cavity flow problem

The flow field driven by a constant upper lid velocity u_{lid} will be investigated in the square cavity at $Re = 3200$ and 5000. Note that $L(=1)$ is chosen as the characteristic length, and $u_{\text{lid}}(=1)$ is the characteristic velocity. The simulated grid-independent mid-plane velocity profiles $u(0.5, y)$ and $v(x, 0.5)$ at two mid-planes are plotted in Figure 4. Good agreement with the benchmark solutions of Ghia *et al.* [14] (■) and Erturk *et al.* [15] (○) confirms the fidelity of the proposed scheme.

5.2. Backward-facing step flow problem

The next problem deals with the incompressible laminar channel flow over a backward-facing step of height h. The downstream channel height $H(=1)$ is equal to $2h$. The downstream channel
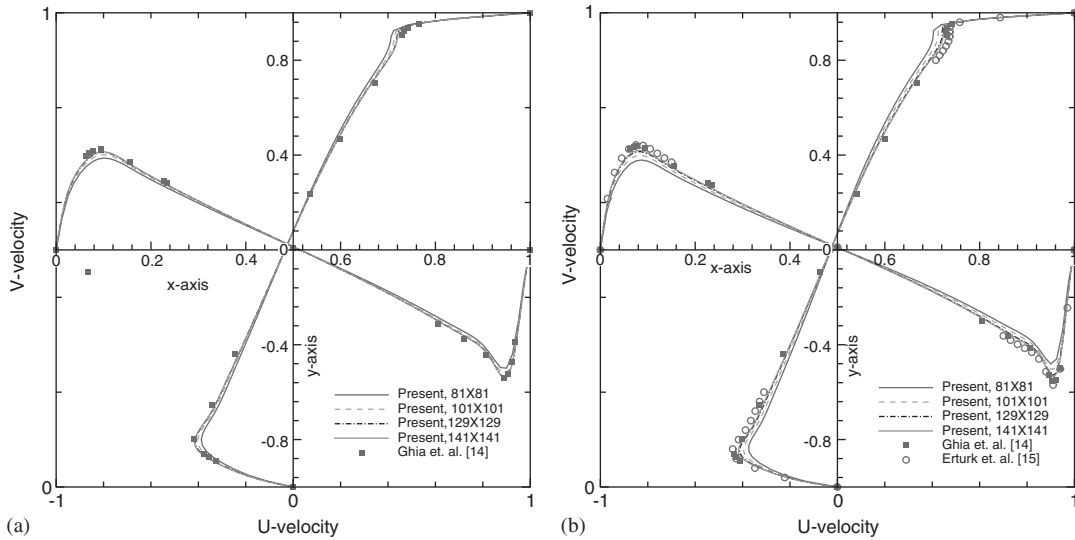
Figure 4. Comparison of the simulated velocity profiles for $u(x, 0.5)$ and $v(0.5, y)$: (a) $Re = 3200$ and (b) $Re = 5000$.
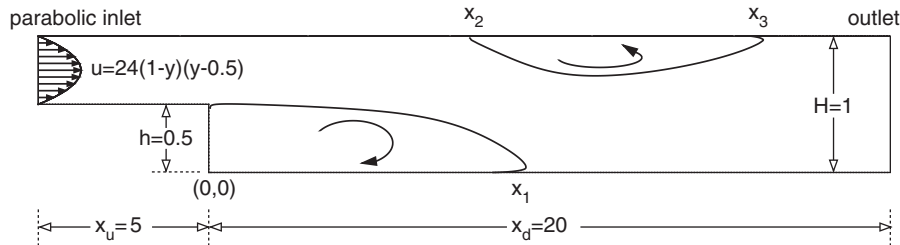

Figure 5. Schematic of the recirculation eddies in the backward-facing step problem considered in Section 5.2.

length is chosen to be $x_d = 40h$, which can yield a traction-free force at the exit [16]. No-slip boundary condition is imposed at the upper and lower boundaries. At the inlet, imposition of $u(0.5 \leqslant y \leqslant 1) = 24(1 - y)(y - 0.5)$ yields the maximum inflow velocity $u_{max} = 1.5$ and an average inflow velocity $u_{avg} = 1$. Denoting x_1 shown in Figure 5 as the reattachment length of the recirculation eddy behind the step. We also define x_2 and x_3 as the separation and reattachment locations of the upper eddy, respectively. The Reynolds number for this investigated problem is defined by the step height h and the average inlet velocity u_{avg}. The predicted lengths of $x_1 \sim x_3$ at $Re = 100, 200, 400, 600$, and 800 are tabulated in Table I, where a grid spacing of $\frac{1}{40}$ was used in each calculation. The simulated solution at $Re = 800$ shows good agreement with the results of Gartling [17] and Keskar and Lyn [18] in Figure 6 for u at $x = 7$ and 15.

Table I. The reattachment and separation locations predicted at different Reynolds numbers. Note that 'no inlet channel' represents the removal of the flow domain defined in $-2 \leqslant x \leqslant 0$ and $1 \leqslant y \leqslant 0.5$. As for the case 'with inlet channel', the flow domain under investigation is the one shown in Figure 5.

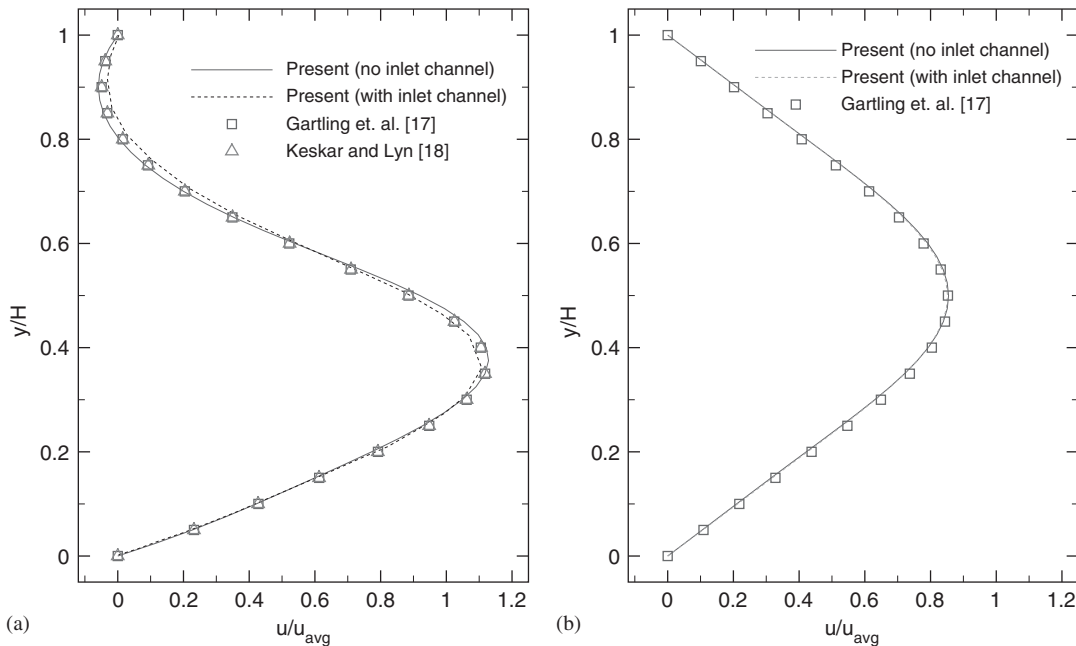|		Re				
		100	200	400	600	800
x_1	Parabolic inlet, no inlet channel	1.5858	2.5906	4.2717	5.3182	6.1405
	Parabolic inlet, with inlet channel	1.4060	2.4971	4.2143	5.2526	5.9950
x_2	Parabolic inlet, no inlet channel	—	—	—	4.2321	4.8054
	Parabolic inlet, with inlet channel	—	—	—	4.1097	4.6677
x_3	Parabolic inlet, no inlet channel	—	—	—	7.8160	10.2202
	Parabolic inlet, with inlet channel	—	—	—	7.8903	10.3569

Figure 6. Comparison of the predicted u velocity profiles at $x = 7$ and 15 with the results given in [17, 18] for the case carried out at $Re = 800$.

6. NUMERICAL RESULTS

6.1. Flow over a circular cylinder

Flow over a circular cylinder has been extensively studied for verifying the IB solvers. At smaller values of Re, the flow is of the diffusion dominated type and is called the creeping flow. At a somewhat higher value of Re (up to $Re = 40$), two symmetrical vortices will be stationarily attached behind the cylinder. When increasing the value of Re, the vortices become stretched and the flow
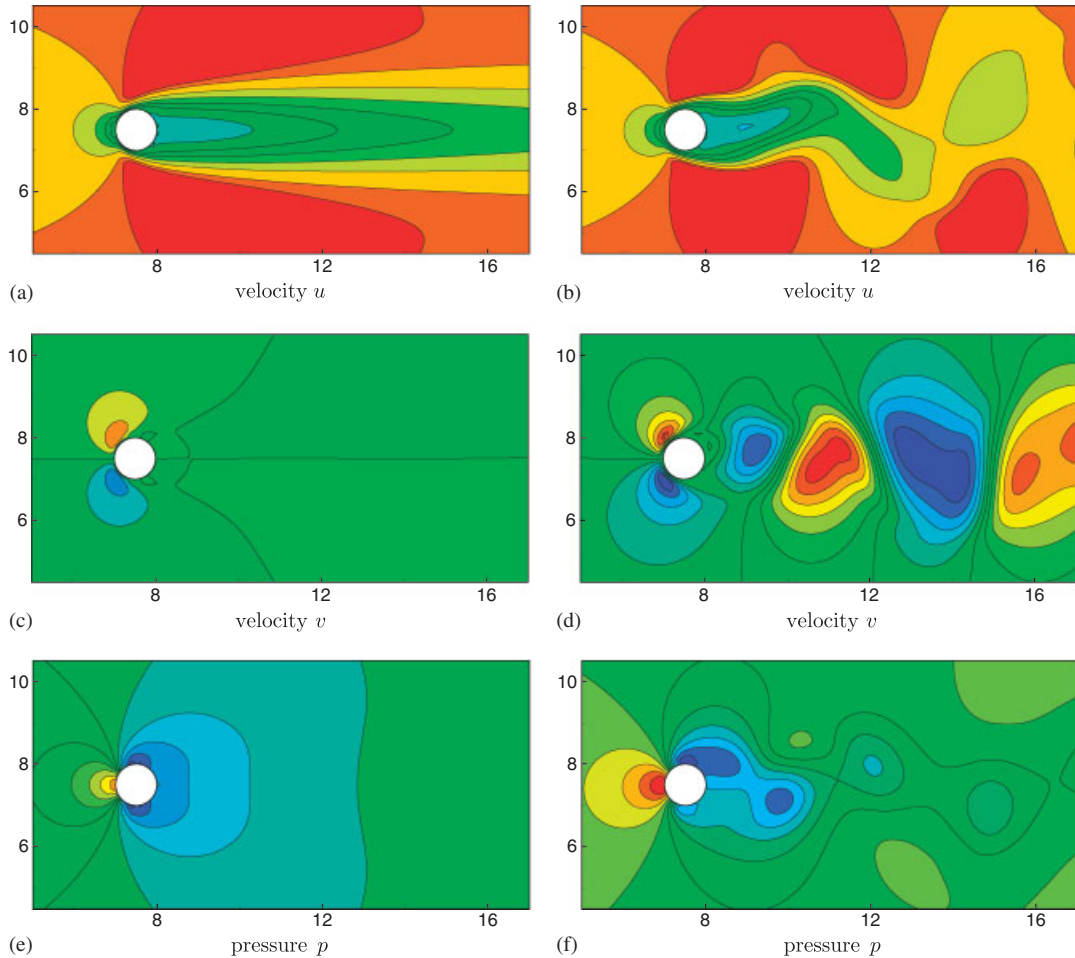
Figure 7. The predicted u, v, p contours near the wake of the circular cylinder at $T = 200$ for the case considered at $Re = 40$ ((a), (c), (e)) and $Re = 80$ ((b), (d), (f)).

will be distorted and broken apart, leading to an alternating vortex shedding (or Kármán vortex street) wake.

In this study, the drag and lift coefficients, and the Strouhal number will be calculated for the sake of comparison with other numerical methods. Drag coefficient is defined as $C_D = F_D/(\frac{1}{2}u_\infty^2 D)$, where $F_D(\equiv -\int_\Omega f_1(\mathbf{x})\,d\mathbf{x} = -\sum_{\mathbf{x}} f_1(\mathbf{x})h^2)$ is the drag force. In the above, $f_1(\mathbf{x})$ is the x-component of the forcing term, and h is the uniform mesh size. Lift coefficient is computed from $C_L = F_L/(\frac{1}{2}u_\infty^2 D)$, where $F_L(\equiv -\int_\Omega f_2(\mathbf{x})\,d\mathbf{x} = -\sum_{\mathbf{x}} f_2(\mathbf{x})h^2)$ is the lift force. Note that $f_2(\mathbf{x})$ is the y-component of the forcing term. When the flow becomes unstable, the stationary vortices behind the cylinder will be evolved to develop the shedding frequency f_q. The dimensionless vortex shedding frequency is called the Strouhal number and is defined as $S_t = f_q/(u_\infty D)$. Denote the dimensionless time period as T_p, S_t can be measured by $S_t = 1/(u_\infty T_p D)$.
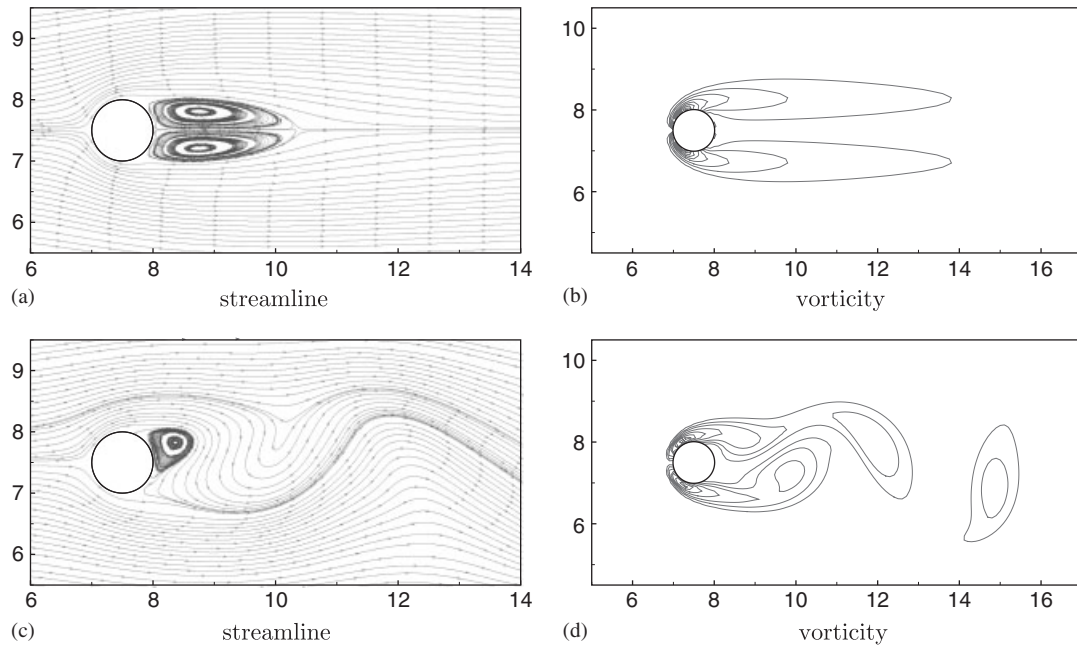
Figure 8. The predicted instantaneous streamlines and vorticity contours in the near wake of the circular cylinder at $T = 200$ for $Re = 40$ ((a) and (b)) and $Re = 80$ ((c) and (d)).

In a rectangular domain, the flow over a stationary cylinder will be simulated in a domain of Cartesian meshes. A constant velocity profile $u_\infty = 1$ was specified at the inlet and the Neumann boundary condition was prescribed along the lateral boundaries. A circular cylinder of diameter $D = 1$ was placed inside the flow domain ($0 \leqslant x \leqslant 30D$, $0 \leqslant y \leqslant 15D$) with its center located at $x = 7.5D$ and $y = 7.5D$. According to the grid refinement study of Lima E Silva *et al.* [19], the mesh with the nodal points of 301×151 is chosen, respectively, in the streamwise (x) and transverse (y) directions. Our simulations were performed at two Reynolds numbers ($Re = (\rho u_\infty D)/\mu = 40, 80$), where the characteristic length and velocity are the diameter of the cylinder (D) and the constant velocity at the inlet (u_∞), respectively. The dimensionless time was defined as $T = (u_\infty t)/D$.

For the case with $Re = 40$, the wake predicted behind the cylinder was seen to reach a steady symmetric state. This predicted result is in good agreement with the well-established result, which was obtained by the linear stability theory. The cylinder wake instabilities can be observed as $Re \geqslant 47$. This is indeed what we predict from the simulation carried out at $Re = 80$. In order to confirm this phenomenon, the ($\mathbf{u}$, p) contours were plotted in the near wake of the circular cylinder at $T = 200$ in Figure 7. Figure 8 shows the streamline vector and the corresponding vorticity fields at $T = 200$ for $Re = 40$ and 80, respectively.

Figure 9 shows the time evolution of the drag and the lift coefficients at $Re = 40$ and 80, respectively. Figure 10 shows the power spectrum of C_L at $Re = 80$. The Strouhal number corresponding to the dominant frequency of lift variation is predicted approximately to be 0.15. The length of the bubble recirculation (L_w) schematic in Figure 11 is defined as the distance between the two
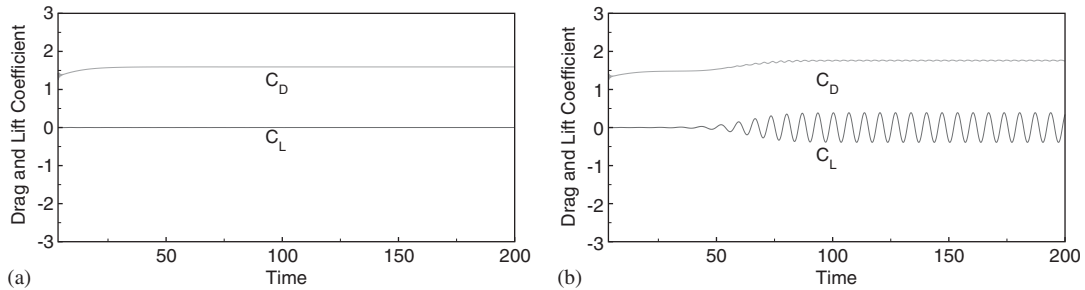
Figure 9. The simulated time-evolving drag and lift coefficients for the
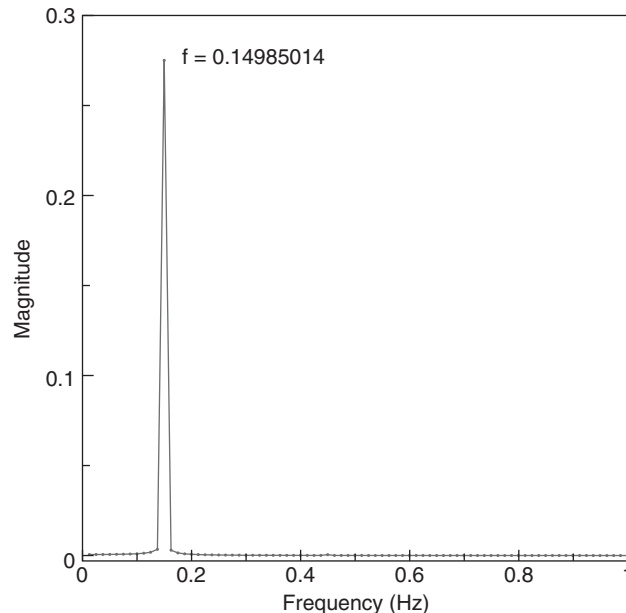flow over a cylinder: (a) $Re = 40$ and (b) $Re = 80$.

Figure 10. The predicted power spectrum of the lift coefficient (C_L) for the flow over a cylinder at $Re = 80$.

stagnation points located downstream of the cylinder. Figure 12 shows these distributions against coordinate x predicted by different IB methods [19, 20] at $Re = 40$.

Comparison of the drag coefficient, length of eddy recirculation, and Strouhal number with other established results obtained at $Re = 40$ and 80 is presented in Table II (including references [8, 19, 21–29]). In this table, the drag coefficients calculated by the Cartesian grid methods were found to have slightly larger values than those obtained from the body-fitted methods. The predicted volume of fluid (VOF) results are noted to be comparatively different from others. The results obtained from the direct forcing method and the currently proposed method are close to the formerly cited results.
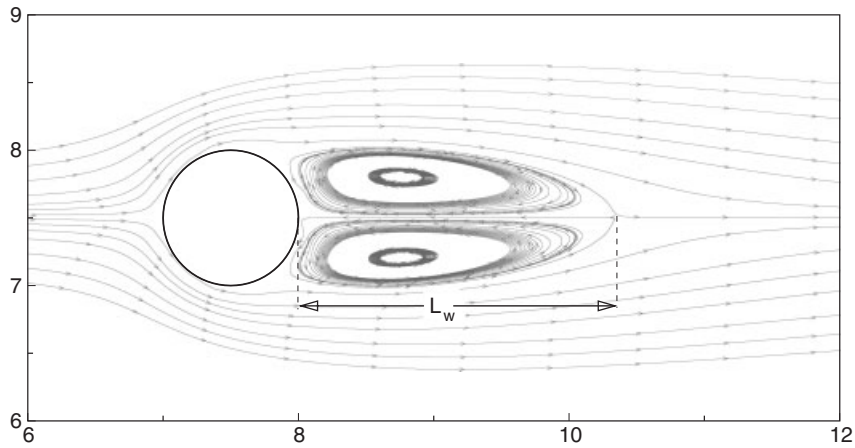
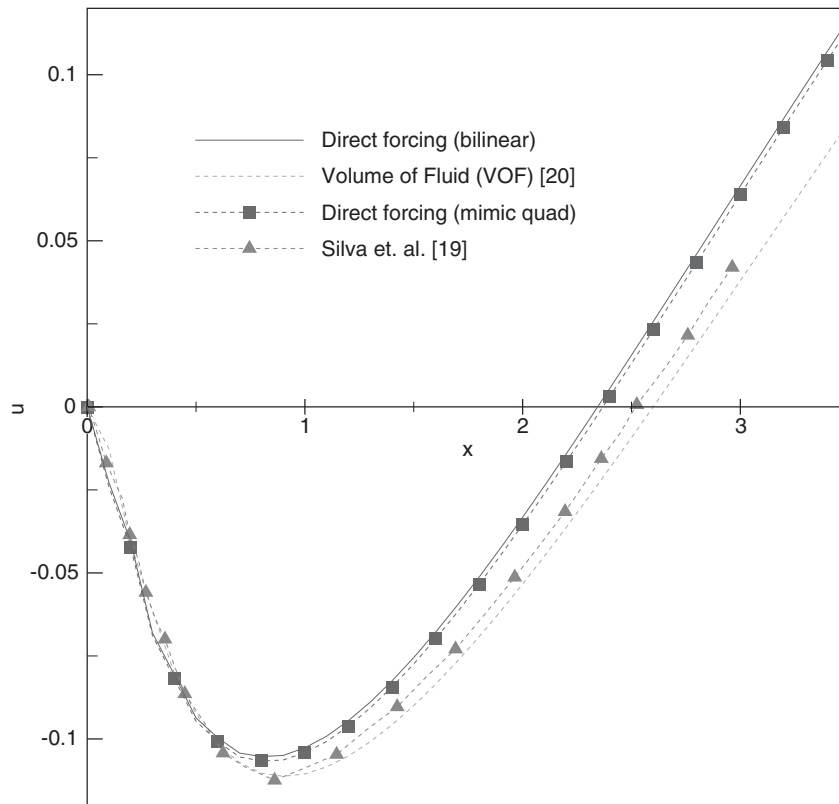Figure 11. Definition of the length of the bubble recirculation.

Figure 12. The plots of the simulated horizontal velocity component (u) against the coordinate x.

Table II. Comparison of the predicted drag coefficient, length of the bubble recirculation, and Strouhal number (frequency) with some other results carried out at $Re = 40$ and 80.

Study	Year	$Re = 40$		$Re = 80$	
		C_D	L_w	C_D	S_t
Tritton [21]*	1959	1.48	—	1.29	—
Dennis and Chang [22][†]	1970	1.52	2.35	—	—
Fornberg [23][†]	1980	1.50	2.24	—	—
Williamson [24, 25]*	1989, 1996	—	—	—	0.15
Park et al. [26][†]	1998	1.51	—	1.35	—
Ye et al. [8][‡]	1999	1.52	2.27	1.37	0.15
Calhoun [27][‡]	2002	1.62	2.18	—	—
Lima E Silva et al. [19][‡]	2003	1.54	—	1.40	0.15
Russell and Wang [28][‡]	2003	1.60	2.29	—	—
Ding et al. [29][§]	2004	1.71	2.20	—	—
This study (VOF)[‡]	2005	1.78	2.55	1.44	0.15
This study (direct forcing—bilinear)[‡]	2005	1.59	2.34	1.39	0.15
This study (direct forcing—mimic quad)[‡]	2005	1.57	2.36	1.37	0.15

*The experimental data.
[†]The numerical data calculated from the body-fitted grid method.
[‡]The numerical data calculated from the Cartesian grid method.
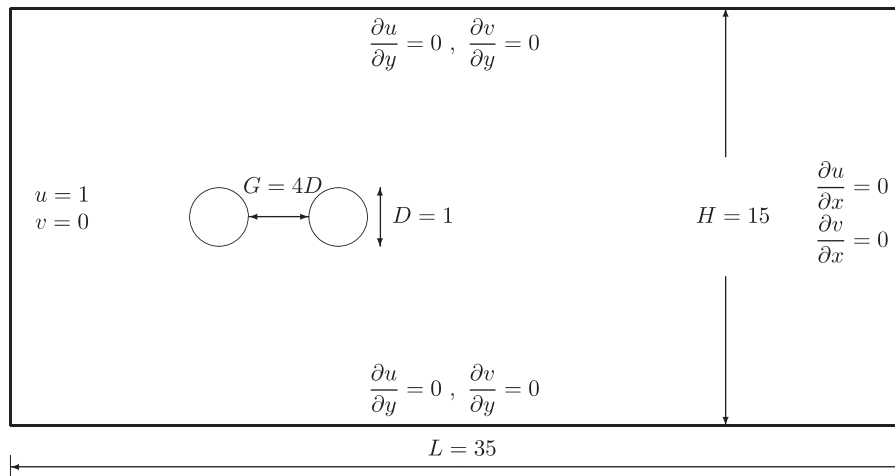[§]The numerical data calculated from the meshless method.

Figure 13. The computational domain and boundary condition for the flow over two cylinders in tandem.

6.2. Flow over two cylinders in tandem

Flow over two cylinders in tandem was simulated in the Cartesian mesh. The distance between the two cylinder surfaces is denoted by the dimensionless value $g^* = G/D$, where G is the minimum

Table III. Comparison of the average drag coefficient, Strouhal number for
the cylinders in tandem at $g^* = 4.0$, $Re = 200$.

Study	C_{D_1}	C_{D_2}	S_{t_1}	S_{t_2}
Farrant *et al.* [31]	1.25	0.38	0.179	0.179
Meneghini *et al.* [32]	1.18	0.38	0.174	0.174
This study (direct forcing—mimic quad)	1.31	0.39	0.171	0.171

Index 1 refers to the upstream circular cylinder, and index 2 indicates the
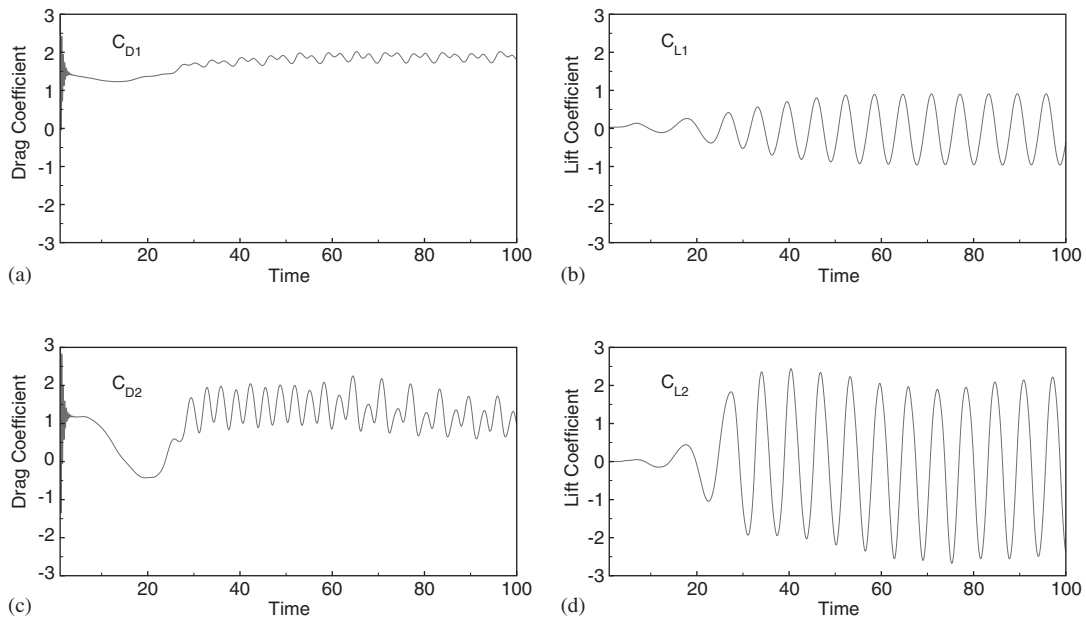downstream circular cylinder.

Figure 14. The time evolution of the drag and lift coefficients for the case considered in Section 6.2:
(a)–(c) drag coefficient and (b)–(d) lift coefficient.

distance between the cylinder surfaces and D is the cylinder diameter. It has been known from the experimental result of Zdravkovich [30] that when the cylinder spacing g^* becomes larger than 3.8, the upstream cylinder will be shed in synchronization with the downstream one. To demonstrate that the current method has the ability to predict the flows in complex geometries, a calculation was performed for the flow over two cylinders in tandem at $Re = 200$ and $g^* = 4.0$.

A constant velocity $u_\infty = 1$ was specified at the inlet and a Neumann boundary condition was prescribed along the lateral boundaries. Two circular cylinders of diameter $D = 1$ were placed inside the domain with their centers located at $(x, y) = (5.5D, 7.5D)$ and $(10.5D, 7.5D)$. The simulations have been carried out in a computational domain ($0 \leqslant x \leqslant 35D$, $0 \leqslant y \leqslant 15D$), schematic in Figure 13, that is sufficiently apart from two cylinders to minimize the boundary effect on the flow development. The grid points are chosen to be 351×151 in the streamwise (x) and transverse (y) directions, respectively.
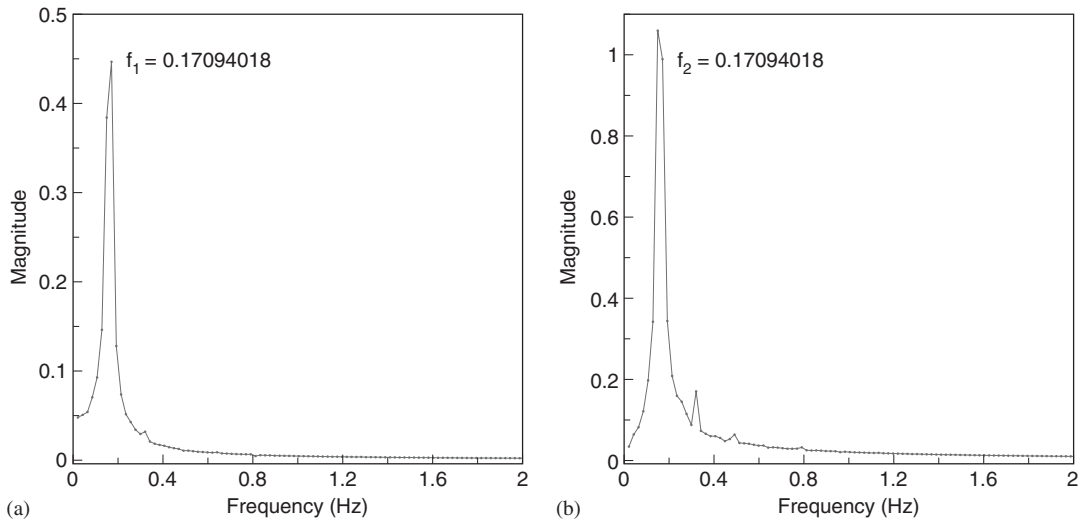
Figure 15. The predicted power spectra of the lift coefficient (C_L) for the flow over two cylinders in tandem: (a) upstream cylinder 1 and (b) downstream cylinder 2.
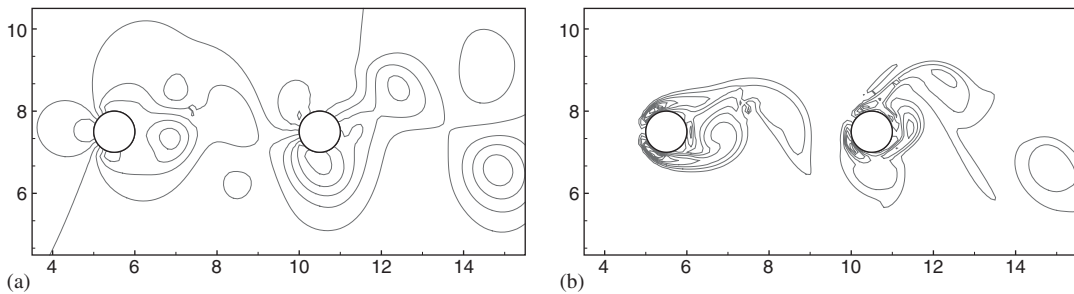

Figure 16. The predicted instantaneous pressure and vorticity contours in the near wake of the circular cylinder at $T = 100$ for $Re = 200$: (a) pressure contours and (b) vorticity contours.

For the investigated cylinders in tandem, the computation was performed at $Re = 200$ and $g^* = 4.0$, which were performed by Farrant *et al.* [31] and Meneghini *et al.* [32]. Comparison of the predicted time-averaged drag coefficient and Strouhal number with the established results is given in Table III. Good agreement with other non-Cartesian numerical simulations confirms that the proposed method implemented in Cartesian grids can be applied to predict the flows in complex geometries.

The drag and lift coefficients against time for both cylinders are plotted in Figure 14, where index 1 refers to the upstream circular, and index 2 represents the downstream circular cylinder. The power spectra of the lift coefficient (C_L) and the Strouhal number for both cylinders corresponding to the dominant frequency of the lift variation with the same value (that is, 0.171) are shown in Figure 15. The identical Strouhal numbers confirm that the shedding is synchronized and their values are in agreement with the experimental data. In order to reveal the behavior of the cylinders in

tandem, the streamline vector, vorticity contours and the corresponding pressure field and vorticity at $T = 100$ are also plotted in Figure 16.

7. CONCLUDING REMARKS

In this study, an IB method is proposed for the simulation of time-dependent (unsteady), incompressible viscous flows over circular cylinder and two cylinders in tandem in Cartesian grids. For the sake of more accurately capturing the shape of the immersed body in the flow, more points at which the momentum forcing terms are added to the momentum equations are involved to simulate the effect of the body in the flow. The drag and lift coefficients, the Strouhal number, the length of bubble recirculation, and the centerline velocities downstream of the cylinder were predicted at two Reynolds numbers ($Re = 40, 80$). The results compare favorably with the experimental and other numerical results.

REFERENCES

1. Peskin CS. Flow patterns around heart valves: a numerical method. *Journal of Computational Physics* 1972; **10**:252–271.
2. Sirovich L. Initial, boundary value problems in dissipative gas dynamics. *Physics of Fluids* 1967; **10**:24–34.
3. Goldstein D, Haandler R, Sirovich L. Modeling a no-slip flow boundary with an external force field. *Journal of Computational Physics* 1993; **105**:354–336.
4. Saiki EM, Biringen S. Numerical simulation of a cylinder in uniform flow: application of a virtual boundary method. *Journal of Computational Physics* 1996; **123**:450–465.
5. Mittal R, Iaccarino G. Immersed boundary methods. *Annual Review of Fluid Mechanics* 2005; **37**:239–261.
6. Mohd-Yusof J. Combined immersed boundary/B-spline method for simulations of flows in complex geometries. *CTR Annual Research Briefs*, NASA Ames/Stanford University, 1997; 317–327.
7. Fadlun EA, Verzicco R, Orlandi P, Mohd-Yusof J. Combined immersed-boundary methods for three dimensional complex flow simulations. *Journal of Computational Physics* 2000; **161**:30–60.
8. Ye T, Mittal R, Udaykumar HS, Shyy W. An accurate Cartesian grid method for viscous incompressible flows with complex immersed boundaries. *Journal of Computational Physics* 1999; **156**:209–240.
9. Wang MMT, Sheu TWH. An element-by-element BICGSTAB iterative method for three-dimensional steady Navier–Stokes equations. *Journal of Computational and Applied Mathematics* 1997; **79**:147–165.
10. Gresho PM, Sani RL. On pressure boundary conditions for the incompressible Navier–Stokes equations. *International Journal for Numerical Methods in Fluids* 1987; **7**:1111–1145.
11. Li CW, Wang LL. An immersed boundary finite difference method for LES of flow around bluff shapes. *International Journal for Numerical Methods in Fluids* 2004; **46**:85–107.
12. Sheu TWH, Lin RK. Newton linearization on the incompressible Navier–Stokes equations. *International Journal for Numerical Methods in Fluids* 2004; **44**:297–312.
13. Sheu TWH, Lin RK. An incompressible Navier–Stokes model implemented on non-staggered grids. *Numerical Heat Transfer, Part B: Fundamentals* 2003; **44**:277–294.
14. Ghia U, Ghia KN, Shin CT. High-*Re* solutions for incompressible flow using the Navier–Stokes equations and a multigrid method. *Journal of Computational Physics* 1982; **48**:387–411.
15. Erturk E, Corke TC, Gökcöl C. Numerical solution of 2-D steady incompressible driven cavity flow at high Reynolds numbers. *International Journal for Numerical Methods in Fluids* 2005; **48**:747–774.

16. Wang MT, Sheu TWH. Implementation of a free boundary condition to Navier–Stokes equations. *International Journal of Numerical Methods for Heat and Fluid Flow* 1997; **7**:95–111.
17. Gartling DK. A test problem for outflow boundary conditions-flow over a backward-facing step. *International Journal for Numerical Methods in Fluids* 1990; **11**:953–967.
18. Keskar J, Lyn DA. Computations of a laminar backward-facing step flow at $Re=800$ with a spectral domain decomposition method. *International Journal for Numerical Methods in Fluids* 1999; **29**:411–427.
19. Lima E Silva ALF, Silverira-Neto A, Damasceno JJR. Numerical simulation of two-dimensional flows over a circular cylinder using the immersed boundary method. *Journal of Computational Physics* 2003; **189**:351–370.
20. Ting HF. Immersed boundary method for solving incompressible viscous flow equations in complex geometry. *Master's Thesis*, Department of Engineering Science and Ocean Engineering, National Taiwan University, 2005.
21. Tritton DJ. Experiments on the flow past a circular cylinder at low Reynolds numbers. *Journal of Fluid Mechanics* 1959; **6**:547–567.
22. Dennis SCR, Chang G. Numerical solutions for steady flow past a circular cylinder at Reynolds number up to 100. *Journal of Fluid Mechanics* 1970; **42**:471–489.
23. Fornberg B. A numerical study of steady viscous flow past a circular cylinder. *Journal of Fluid Mechanics* 1980; **98**:819–855.
24. Williamson CHK. Oblique and parallel modes of vortex shedding in the wake of a circular cylinder at low Reynolds numbers. *Journal of Fluid Mechanics* 1989; **206**:579–627.
25. Williamson CHK. Vortex dynamics in the cylinder wake. *Annual Review of Fluid Mechanics* 1996; **28**:477–539.
26. Park J, Kwon K, Choi H. Numerical solutions of flow past a circular cylinder at Reynolds number up to 160. *KSME International Journal* 1998; **12**:1200–1205.
27. Calhoun D. A Cartesian grid method for solving the two-dimensional streamfunction–vorticity equations in irregular regions. *Journal of Computational Physics* 2002; **176**:231–275.
28. Russell D, Wang ZJ. A Cartesian grid method for modeling multiple moving object in 2D incompressible viscous flow. *Journal of Computational Physics* 2003; **191**:177–205.
29. Ding H, Shu C, Yeo KS, Xu D. Simulation of incompressible viscous flows past a circular cylinder by hybrid FD scheme and meshless least square-based finite difference method. *Computer Methods in Applied Mechanics and Engineering* 2004; **193**:727–744.
30. Zdravkovich MM. Review of flow interference between two circular cylinders in various arrangements. *Journal of Fluids Engineering* 1977; **99**:618–633.
31. Farrant T, Tan M, Tan WG. A cell boundary element method applied to laminar vortex shedding from circular cylinders. *Computers and Fluids* 2001; **30**:211–236.
32. Meneghini JR, Saltara F, Siqueira CLR, Ferrari JA. Numerical simulation of flow interference between two circular cylinders in tandem and side-by-side arrangements. *Journal of Fluids and Structures* 2001; **15**:327–350.